Respiratory Research

RESEARCH

Open Access

Intranasal delivery of R8-modified circNFXL1 liposomes ameliorates Su5416-induced pulmonary arterial hypertension in C57BL/6 mice

Shan-Shan Li[1*†], Miao Guo[1†], Ying Zhao[1†], Feifei Fan[1], Shaoyuan Huang[1], Houzhi Yang[4], Xu Chen[2,3] and Xin Jin[1,2,3*]

Abstract

Background Pulmonary arterial hypertension (PAH) is a progressive, life-threatening condition characterized by increased pulmonary vascular resistance and right ventricular hypertrophy (RVH). Current treatments primarily alleviate symptoms but do not effectively target the underlying molecular mechanisms driving the disease. This study aimed to evaluate the therapeutic potential of R8-modified liposomal delivery of circNFXL1, a circular RNA, in a mouse model of PAH.

Methods R8-circNFXL1 liposomes were synthesized and characterized for their physicochemical properties, including encapsulation efficiency. PAH was induced in C57BL/6 mice using a combination of subcutaneous Su5416 administration and hypoxic exposure. Intranasal delivery of R8-circNFXL1 was performed, and therapeutic effects were assessed using echocardiography and hemodynamic measurements. Molecular mechanisms were explored through analysis of the miR-29b/Kcnb1 axis, a regulatory pathway in PAH.

Results The R8-circNFXL1 liposomes demonstrated optimal physicochemical properties, including high encapsulation efficiency. Treatment with R8-circNFXL1 significantly reduced RVH, improved cardiac function, and mitigated pulmonary vascular remodeling compared to untreated PAH controls. Molecular analysis revealed that R8-circNFXL1 modulated the miR-29b/Kcnb1 axis, providing insights into its mechanism of action.

Conclusions R8-circNFXL1 liposomes offer a promising, targeted therapeutic strategy for PAH by addressing underlying molecular mechanisms. This approach has potential implications for developing alternative treatments to improve disease management and outcomes in PAH.

Keywords Pulmonary arterial hypertension, circNFXL1, Liposomal delivery, Intranasal administration

†Shan-Shan Li, Miao Guo, and Ying Zhao contributed equally to this study.

*Correspondence:
Shan-Shan Li
shanshan.li@nankai.edu
Xin Jin
xin.jin@nankai.edu.cn
Full list of author information is available at the end of the article

Background

PAH is a severe, progressive disorder characterized by elevated pulmonary arterial pressure, leading to right ventricular hypertrophy and eventual heart failure [1, 2]. The pathophysiology of PAH involves a complex interplay of mechanisms, including endothelial dysfunction, smooth muscle cell proliferation, and inflammatory responses, which contribute to thickened arterial walls, narrowed vascular lumens, and increased vascular resistance [3–5]. Although current pharmacological treatments, such as calcium channel blockers, endothelin receptor antagonists, prostacyclin analogs, and phosphodiesterase-5 inhibitors, function primarily as vasodilators, they fail to reverse vascular remodeling or halt disease progression [1, 6]. Therefore, there is an urgent need for novel therapies that target the molecular drivers of PAH and potentially alter its course.

Recent advances in molecular biology have highlighted the critical role of non-coding RNAs in PAH pathophysiology, influencing vascular remodeling, apoptosis resistance, and smooth muscle proliferation [7–9]. Among these, circular RNAs (circRNAs) have attracted significant attention due to their inherent stability and specific expression patterns in various tissues and diseases [10–12]. Our previous research identified that circNFXL1 is significantly downregulated in PAH patients with chronic obstructive pulmonary disease and in hypoxia-exposed human pulmonary artery smooth muscle cells (PASMCs) [13]. This downregulation correlates with increased PASMC proliferation and migration and reduced apoptosis, key features of PAH-associated vascular remodeling. Mechanistically, circNFXL1 functions as a molecular sponge for hsa-miR-29b-2-5p, a microRNA that negatively regulates voltage-gated potassium channel subfamily B member 1 (KCNB1) [13, 14]. Given these findings, we hypothesized that restoring circNFXL1 levels in pulmonary tissues could counteract pathological vascular remodeling and attenuate PAH progression. However, the efficient and targeted delivery of therapeutic circRNAs remains a major challenge due to RNA instability and poor cellular uptake. To address this, we developed a liposomal delivery system optimized for circNFXL1 delivery to the pulmonary vasculature.

Liposomes, small spherical vesicles composed of phospholipid bilayers, are well-established therapeutic carriers that enhance drug solubility, protect RNA molecules from degradation, and enable controlled release [15]. By engineering liposomes with optimized size, composition, and surface modifications, including polyethylene glycol (PEG) for prolonged circulation and immune evasion, we aimed to maximize the pulmonary delivery of circNFXL1 [16].

To further enhance cellular uptake, we incorporated octa-arginine (R8), a well-characterized cell-penetrating peptide (CPP) known for its ability to facilitate intracellular transport [17]. The strong positive charge of R8 promotes efficient interactions with negatively charged cell membranes, thereby enhancing the intracellular delivery of liposomal contents [18]. In this study, we conjugated R8 to the liposome surface (R8-PEG2000) to optimize the intranasal delivery of circNFXL1, ensuring targeted pulmonary localization with minimal systemic exposure. This R8-PEG2000-modified liposomal system offers multiple advantages, including enhanced bioavailability, improved intracellular uptake, and the ability to bypass biological barriers. We evaluated its therapeutic efficacy in a PAH mouse model, focusing on its impact on RVH, vascular remodeling, and overall cardiac function. By targeting circRNA-driven regulatory pathways, this study introduces a novel and mechanistically distinct therapeutic strategy for PAH management, with potential clinical implications for RNA-based interventions.

Materials and methods

Animals

All animal procedures were approved by the Nankai University Animal Care and Use Committee, Beijing, China. Eight-week-old male C57BL/6 mice, each weighing approximately 20 ± 2 g, were sourced from SPF Biotechnology Co., Ltd., Beijing, China. Before the start of the experiment, the mice were acclimatized for one week in a controlled environment, with bedding replaced regularly to maintain a clean habitat. Throughout the study, the mice had ad libitum access to standard rodent chow and water. During the experiment, specific environmental conditions were maintained, including a 12-h light/dark cycle, stable room temperature, and humidity levels in compliance with institutional animal welfare guidelines.

R8-PEG2000 liposome (R8-PEG2000-Lip) preparation

To prepare R8-PEG2000 liposomes, soy lecithin (SPC), cholesterol (Chol), DSPE-PEG2000, and DSPE-PEG2000-R8 were mixed in a molar ratio of 59:33:3:5. A total of 10 μmol of this lipid mixture was dissolved in anhydrous ethanol to form the lipid phase. Using a rotary evaporator, the solution was evaporated under reduced pressure to create a thin lipid film on the walls of the flask, which was subsequently incubated at 4 °C for 2 h to stabilize the lipid membrane. Following incubation, the lipid film was rehydrated with 3 mL of phosphate-buffered saline (PBS) and incubated in a 60 °C water bath for 45 min to achieve complete hydration. The lipid suspension was then subjected to

intermittent probe sonication at 100 watts for a total of 10 min to reduce particle size. After sonication, the suspension was filtered through a 0.22-μm sterile filter to ensure sterility, resulting in a final concentration of approximately 10 μmol in 2.5 mL of R8-PEG2000-Lip suspension. Parallelly, PEG2000 liposomes without R8 modification were prepared by dissolving SPC, Chol, and DSPE-PEG2000 in anhydrous ethanol at a molar ratio of 76:19:5. Similar to the R8-modified liposome preparation, the mixture was evaporated to form a thin lipid film, rehydrated with 3 mL PBS, and subjected to identical sonication and filtration processes. The resulting PEG2000-Lip suspension was also obtained at a concentration of approximately 10 μmol in 2.5 mL.

Synthesis of R8-PEG2000 lipid conjugate

The R8-PEG2000 lipid conjugate was synthesized by combining Octaarginine (R8) peptide with DSPE-PEG2000-Mal in a chloroform/methanol solution (2:1 v/v) at a molar ratio of 1.5:1. The reaction was facilitated by adding triethylamine as a catalyst and was gently stirred at room temperature for 48 h. Following the reaction, the solvent mixture was evaporated under reduced pressure to obtain a precipitate. The precipitate was re-dissolved in chloroform, filtered to isolate the DSPE-PEG2000-R8 complex, and further concentrated by vacuum evaporation at 40 °C to form a thin R8-PEG2000 lipid membrane.

Assembly of circNFXL1 liposomal complexes

The recombinant circNFXL1 expression vector was previously constructed in our laboratory, and circularization of circNFXL1 was confirmed by quantitative reverse transcription PCR (qRT-PCR) and Sanger sequencing. The purified circNFXL1 was then complexed with either R8-PEG2000-Lip or PEG2000-Lip by incubating 5 mg of circNFXL1 with 2.5 mL of 10 μmol liposomal suspension at 4 °C for 2 h. This assembly resulted in R8-PEG2000-Lip-modified circNFXL1 (R8-circNFXL1) and PEG2000-Lip-modified circNFXL1 (Lip-circNFXL1), both prepared at a final concentration of 2 mg/mL. The assembled complexes were subsequently diluted in PBS to various concentrations for downstream applications.

Morphological and physicochemical characterization of liposomes

Morphological examination of the R8-circNFXL1 and Lip-circNFXL1 liposomal formulations was conducted using transmission electron microscopy (TEM) on an HT7800 series TEM instrument (Hitachi High-Tech, Japan). Copper grids were prepared by placing them on individual pieces of filter paper. A 10 μL aliquot of each liposomal formulation (0.5 mg/mL) was applied to the surface of the grid and allowed to stand for 30 min to facilitate adsorption. Excess liquid was gently blotted with filter paper, ensuring a dry surface. This drying process was repeated three times to guarantee complete sample preparation. The grids were then stained with 2% (w/v) phosphotungstic acid for 30 s, followed by air drying at room temperature overnight. TEM imaging was performed to capture high-resolution images of the liposomal morphology.

The particle size, polydispersity index (PDI), and zeta potential (ZP) of R8-circNFXL1 and Lip-circNFXL1 were determined using dynamic light scattering (DLS) and zeta potential analysis. Particle size and PDI measurements were performed on a Zetasizer Nano S90 (ZEN1690, Malvern Instruments, Malvern, UK) with each liposomal formulation diluted to the appropriate concentration in ultrapure water. Each sample was analyzed in triplicate at 25 °C with a detection angle of 90° and a wavelength of 633 nm, and results were averaged for accuracy. Zeta potential measurements were conducted on a ZETAPALS/BI-200SM instrument (Brookhaven Instruments, Holtsville, NY, USA) equipped with an electrode for accurate charge determination under the same conditions as the DLS measurements.

Encapsulation efficiency and enzyme digestion validation

To quantify the total DNA content (CT) in the liposome formulation, 0.2 mL of the liposome suspension was mixed with 3 mL of 10% Triton X-100 solution. To measure the free, unencapsulated DNA content (CF), another 0.2 mL of the liposome suspension was subjected to high-speed centrifugation for 1.5 h. Following centrifugation, 0.2 mL of the resulting supernatant was mixed with Triton X-100, and the total volume was adjusted to 3 mL. Absorbance measurements of all samples were taken at 260 nm using a UV spectrophotometer. The encapsulation efficiency was calculated using the formula: $(CT - CF)/CT \times 100\%$.

To confirm successful encapsulation, both the unencapsulated circNFXL1 plasmid and various concentrations of liposomal circNFXL1 were digested with EcoRI and BamHI for 2 h. Digestion products were subsequently analyzed by agarose gel electrophoresis to assess DNA integrity and verify encapsulation. The stability of liposomal circNFXL1 was evaluated by storing the formulation in capillary vials at 4 °C. Particle size and polydispersity index (PDI) were measured daily for 7 days to monitor stability. All tests were conducted in triplicate to ensure accuracy and reproducibility.

Hemolysis assay

To evaluate the hemolytic potential of liposomal circNFXL1, 1 mL of heparinized blood was mixed with 7 mL of phosphate-buffered saline (PBS) and centrifuged to remove the supernatant. This washing step was repeated three times to ensure purity. Afterward, 40 μL of isolated red blood cells (RBCs) was resuspended in 960 μL of PBS to prepare a 4% (v/v) RBC suspension, which served as the negative control. Distilled water was used as the positive control.

For each experimental group, 40 μL of RBC suspension was mixed with 960 μL of liposomal circNFXL1 at varying concentrations. Samples were incubated at 37 °C for 30 min, followed by centrifugation to separate the supernatant. A 200 μL aliquot of the supernatant was then transferred to a 96-well plate, and absorbance was measured at 545 nm using a spectrophotometer. Hemolysis (%) = (Sample OD − Negative OD)/(Positive OD − Negative OD) × 100%.

In vivo and ex vivo optical imaging

Liposomal circNFXL1 was labeled with the lipophilic carbocyanine dye DiIC18(5)-DS (DID) by mixing an equal volume of the liposome preparation with a 5 μM DID solution and incubating at 4 °C for 2 h. The labeled formulation was then administered intranasally to mice. For in vivo imaging, mice were randomly divided into three groups: Free DID (DID dye alone, unassociated with liposomes), PLC5-DID (R8-PEG2000-Lip or PEG2000-Lip coated PLC5 vector labeled with DID), and liposomal circNFXL1-DID (R8-circNFXL1 or Lip-circNFXL1 labeled with DID). Imaging was performed at 1, 6, 12, and 24 h post-administration using a small animal live imaging system. Chemiluminescence imaging was conducted with an excitation wavelength of 640 nm.

At 24 h post-administration, the animals were euthanized, and major organs were harvested for ex vivo imaging analysis. Images of the organs were captured using the CCD camera of the Quick View 3000 imaging system (Bio-Real, Austria) to assess biodistribution.

Induction of pulmonary arterial hypertension and R8-circNFXL1 treatment in mice

Eight-week-old C57BL/6 mice were acclimated to standard laboratory conditions for one week before experimental procedures. Mice were then randomly assigned to control and experimental groups: Normal, PAH, and R8-circNFXL1 treatment groups.

To induce PAH, a combination of vascular endothelial growth factor receptor antagonist Su5416 and chronic hypoxia was used. Su5416 was prepared by dissolving in DMSO to a concentration of 20 mg/kg. This solution was administered subcutaneously to the PAH and R8-circNFXL1 groups on days 1, 7, and 14. Following the first Su5416 injection, mice were exposed to a hypoxic environment (10% O_2) for three weeks in a controlled hypoxia chamber to facilitate the development of PAH. The control group received equivalent subcutaneous volumes of DMSO without hypoxia exposure.

Intranasal administration was performed as a noninvasive approach to achieve direct pulmonary targeting. Mice were anesthetized via intraperitoneal injection of 4% (w/v) tribromoethanol and positioned in a supine position at a 45° inclination to facilitate optimal inhalation and lung deposition. On days 07, 14, and 21 of the experimental timeline, R8-circNFXL1 (0.5 mg/mL in PBS) or PBS vehicle control was administered intranasally using a sterile 200 μL micropipette tip. A total volume of 50 μL per nostril was instilled dropwise onto the external nasal vestibule, allowing spontaneous inhalation during normal respiration. To ensure maximal deposition into the respiratory tract, mice were maintained in the inclined position for 30 s post-administration before being returned to their cages. After administration, mice were monitored until fully recovered from anesthesia and returned to their home cages.

Echocardiographic and hemodynamic evaluation

On day 21, mice underwent comprehensive echocardiographic and hemodynamic assessments to evaluate the progression of PAH and associated cardiac function. Cardiac function and hemodynamics were evaluated using transthoracic echocardiography with the VisualSonics Vevo 2100 Micro-Ultrasound system (VisualSonics, Toronto, Canada). Mice were anesthetized with isoflurane and had their chest area depilated to ensure optimal ultrasound transmission. Each mouse was positioned in a supine position on a heated pad to maintain body temperature and limb electrodes were attached to monitor electrocardiographic signals.

Pulmonary artery function was assessed using Pulsed Doppler mode (B-mode), specifically focusing on lung velocity distribution and right ventricular structure. Key parameters measured included: (1) Pulmonary artery acceleration time (PAT); (2) Pulmonary artery ejection time (PET); (3) Maximum pulmonary artery blood flow velocity (PVmax); (4) Pulmonary artery velocity–time integral (PAVIT). Right ventricular structure and function were further evaluated using M-mode imaging in the short-axis view at the level of the aorta. Parameters recorded included: (1) Tricuspid annular plane systolic excursion (TAPSE); (2) Right ventricular cardiac output (CO).

H&E staining

To assess tissue morphology, organs from the mice were fixed in 4% paraformaldehyde (PFA) for 48 h at room temperature. Following fixation, tissues were dehydrated through a graded ethanol series and subsequently cleared in xylene until fully transparent. Tissues were then embedded in paraffin wax, and 5–6 μm thick sections were prepared using a microtome. For staining, paraffin-embedded sections were deparaffinized, rehydrated, and distilled. Prepared slides were examined and photographed under a light microscope to document detailed tissue morphology.

Fulton index analysis for right ventricular hypertrophy

To assess right ventricular hypertrophy (RVH), the hearts were carefully harvested post-mortem from mice under sterile conditions. Each heart was dissected to isolate the right ventricle (RV), left ventricle (LV), and septum (S). The Fulton Index, a validated measure of RVH commonly used in experimental models of pulmonary arterial hypertension, was calculated by weighing the RV separately and comparing it to the combined weight of the LV and S. The Fulton Index was expressed as $RVH = RV/(LV + S)$.

Immunofluorescence staining and fluorescence in situ hybridization

Paraffin-embedded lung tissue sections were first deparaffinized in xylene and rehydrated through a graded ethanol series. Antigen retrieval was performed by heating the sections in 0.01 M ethylenediaminetetraacetic acid (EDTA) buffer at 98 °C for 10 min. After retrieval, sections were incubated overnight at 4 °C in the dark with primary antibodies against α-SMA (Beta Actin, Rabbit, Proteintech) or KCNB1 (Rabbit, Signal Antibody). The following day, sections were treated with horseradish peroxidase (HRP)-conjugated secondary antibodies (Coralight594-, Coralight488-, or Coralight647-conjugated Goat Anti-Rabbit IgG, Proteintech) for 1 h, followed by DAPI staining for 10 min in the dark to visualize nuclei. After thorough washing with phosphate-buffered saline (PBS), sections were mounted with an anti-fade mounting medium and sealed with a coverslip.

To assess the expression and localization of circNFXL1 and miR-29b, we employed RNA-fluorescence in situ hybridization (RNA-FISH) using a cyanine dye-labeled red fluorescent probe for circNFXL1 and a green FAM-labeled fluorescent probe for miR-29b (GenePharma Co., Ltd., Shanghai, China). The hybridization was performed using a fluorescent in situ hybridization kit (GenePharma) according to the manufacturer's instructions. Following hybridization, nuclei were counterstained with 4,6-diamidino-2-phenylindole (DAPI) to enable clear visualization of cellular structures. Fluorescent images were captured using a fluorescence microscope (model to be specified) equipped with appropriate filters for red, green, and blue channels, allowing for detailed analysis of circNFXL1, miR-29b, and KCNB1 expression.

Western blot analysis

Mouse lung tissues were homogenized and lysed on ice in RIPA buffer (Thermo Scientific) containing 1% PMSF. After a 30-min incubation on ice, lysates were centrifuged at 12,000 rpm for 15 min at 4 °C to remove debris. Supernatant protein concentrations were determined via BCA assay (Thermo Scientific). Equal protein amounts (20–40 μg) were prepared with 6×SDS loading buffer, heated at 95 °C for 5 min, and separated on a 4–12% Tris–Glycine SDS-PAGE gel (Invitrogen). Proteins were transferred to PVDF membranes (Thermo Scientific), which were blocked in 5% non-fat milk in TBST for 2 h at room temperature. Membranes were incubated overnight at 4 °C with primary antibodies (KCNB1 primary antibody (Rabbit), Signal antibody), followed by three washes in TBST. HRP-conjugated goat anti-rabbit IgG secondary antibodies (Dako) were applied at 1:10,000 in 5% non-fat milk for 1 h. After further washing, protein bands were detected using ECL substrate (Thermo Scientific) and imaged on a LI-COR Odyssey system (LI-COR Biosciences). Band intensity was analyzed and normalized to β-actin as a loading control.

Quantitative reverse transcription polymerase chain reaction (qRT-PCR)

Total RNA was extracted from mouse lung tissues using an RNA isolation kit (Thermo Scientific) according to the manufacturer's protocol to ensure high purity and integrity. RNA concentration and quality were assessed spectrophotometrically, and RNA integrity was confirmed by agarose gel electrophoresis. For complementary DNA (cDNA) synthesis, 1 μg of total RNA was reverse-transcribed using a cDNA reverse transcription kit (Applied Biosystems) in a final reaction volume of 20 μL. The cDNA was stored at −20 °C until further use. Gene-specific primers were designed for circNFXL1, miR-29b, and Kcnb1. β-actin was used as the internal normalization control for circNFXL1 and Kcnb1, while U6 small nuclear RNA was used as the reference gene for miR-29b quantification qRT-PCR was performed using a SYBR Green master mix (Applied Biosystems) in a real-time PCR system (Thermo Fisher Scientific). Relative gene expression levels for circNFXL1, miR-29b, and Kcnb1 were calculated using the $2^{-\Delta\Delta Ct}$ method.

Statistical analysis

All statistical analyses were performed using GraphPad Prism software (version 9.0). Data are presented as mean ± standard error of the mean (SEM). For pairwise comparisons, an unpaired Student's *t*-test was used. For comparisons involving multiple groups, one-way ANOVA was conducted, followed by Bonferroni's post hoc test to adjust for multiple comparisons. Statistical significance was set at $p < 0.05$.

Results

Construction and characterization of liposomal circNFXL1

The liposomal circNFXL1 delivery system was constructed using a thin-film hydration method (Fig. 1A). Structural lipids, including lecithin and cholesterol, were combined with functionalized lipids, DSPE-PEG2000 or DSPE-PEG2000-R8, in an anhydrous ethanol solution. This mixture was used to form a thin lipid film, which was subsequently rehydrated,

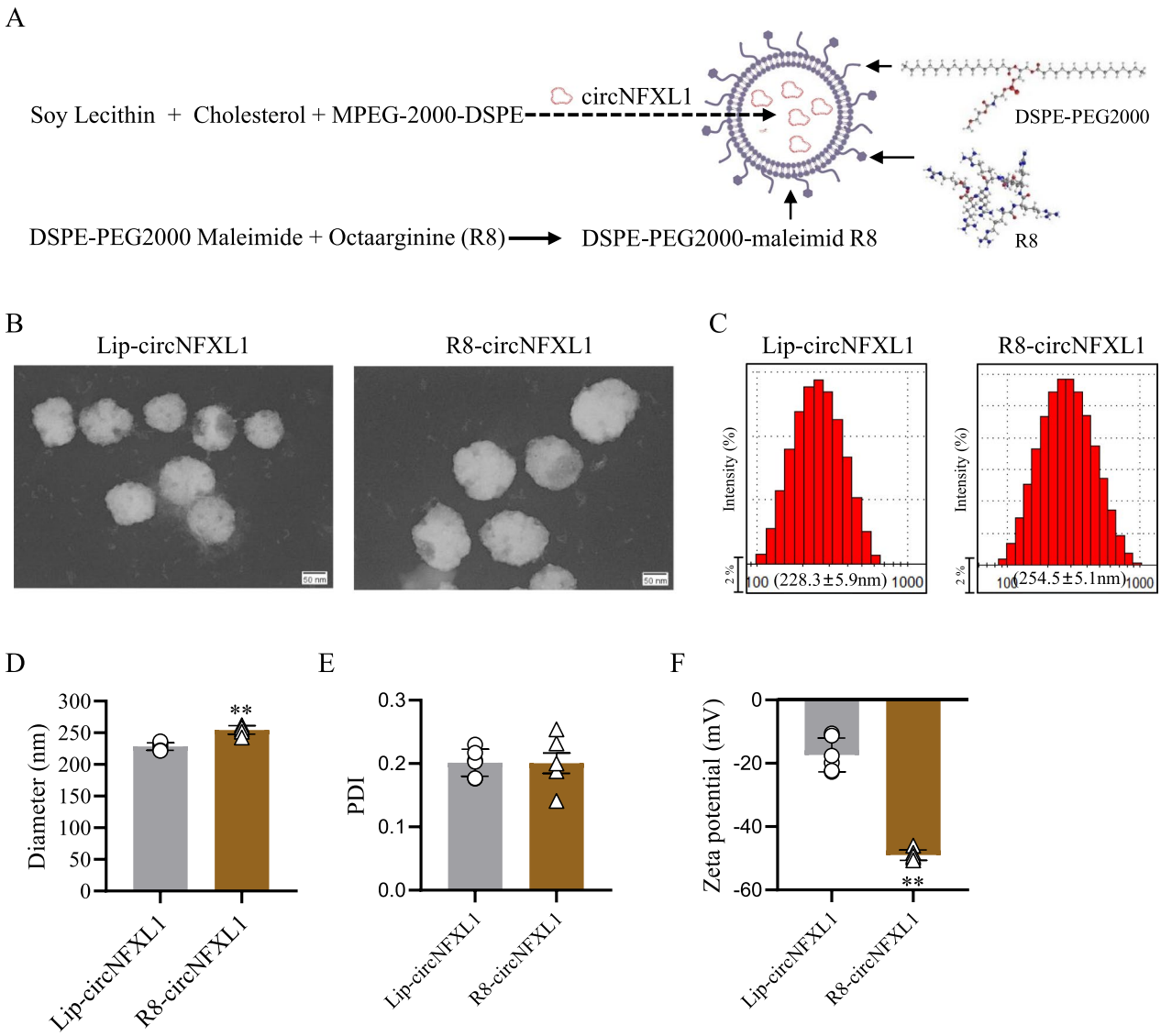

Fig. 1 Synthesis and Characterization of R8-PEG2000 Liposomal circNFXL1 for Targeted Pulmonary Delivery. **A** Schematic representation of the preparation of R8-PEG2000-modified liposomal circNFXL1 (R8-circNFXL1). **B** Transmission electron microscopy (TEM) images of Lip-circNFXL1 (*left*) and R8-Lip-circNFXL1 (*right*), show uniform, spherical structures with well-defined edges, indicative of stable vesicle formation. **C** Dynamic light scattering (DLS) analysis of particle size distribution. **D** The average size of Lip-circNFXL1 is 228.3 ± 5.9 nm, while R8-Lip-circNFXL1 exhibits an average size of 254.5 ± 5.1 nm. **E** Polydispersity index (PDI) values for Lip-circNFXL1 and R8-Lip-circNFXL1. **F** Zeta potential measurements show a significant increase in the negative surface charge for R8-Lip-circNFXL1 compared to Lip-circNFXL1. Data are presented as mean ± SEM. Statistical comparisons were conducted using Student's *t*-test for pairwise comparisons. n = 6 per group. $^{**}p < 0.01$ compared to the Lip-circNFXL1 group

extruded, and dialyzed to yield liposomes encapsulating circNFXL1.

Transmission electron microscopy (TEM) images confirmed the successful formation of liposomal structures for both Lip-circNFXL1 (Fig. 1B, left) and R8-circNFXL1 (Fig. 1B, right), displaying uniform, spherical morphology with well-dispersed particles. Both types of liposomes exhibited smooth surfaces and defined edges, indicative of stable and well-formed vesicles. Dynamic light scattering (DLS) analysis (Fig. 1C) showed that Lip-circNFXL1 had an average particle size of 228.3 ± 5.9 nm, while the R8-circNFXL1 had a slightly larger average size of 254.5 ± 5.1 nm (Fig. 1D). Both formulations demonstrated excellent size uniformity, as indicated by their low polydispersity index (PDI) values. Specifically, Lip-circNFXL1 had a PDI of 0.20 ± 0.02, while R8-circNFXL1 showed a PDI of 0.20 ± 0.04 (Fig. 1E). Zeta potential measurements revealed significant differences in surface charge between the two liposome types. Lip-circNFXL1 exhibited a zeta potential of −17.38 ± 1.99 mV, whereas R8-circNFXL1 had a much higher negative charge, with a zeta potential of −48.99 ± 0.62 mV (Fig. 1F). These results demonstrate that the R8-circNFXL1 formulation possesses favorable physicochemical characteristics for potential therapeutic application in vivo.

Encapsulation efficiency, stability, and safety profile of liposomal circNFXL1 formulations

As shown in Fig. 2A, B, Lip-circNFXL1 achieved encapsulation efficiencies of 83.52 ± 2.45% at 0.5 mg/mL and 86.41 ± 2.52% at 1 mg/mL, while R8-circNFXL1 exhibited even higher efficiencies, reaching 92.16 ± 1.12 and 90.90 ± 2.57% at the same concentrations, suggesting the robust encapsulation capabilities of both liposomal formulations, with the R8-modified liposomes achieving superior efficiency.

To evaluate the formulations' protective efficacy against enzymatic degradation, liposomal circNFXL1 samples were exposed to EcoRI and BamHI endonucleases.

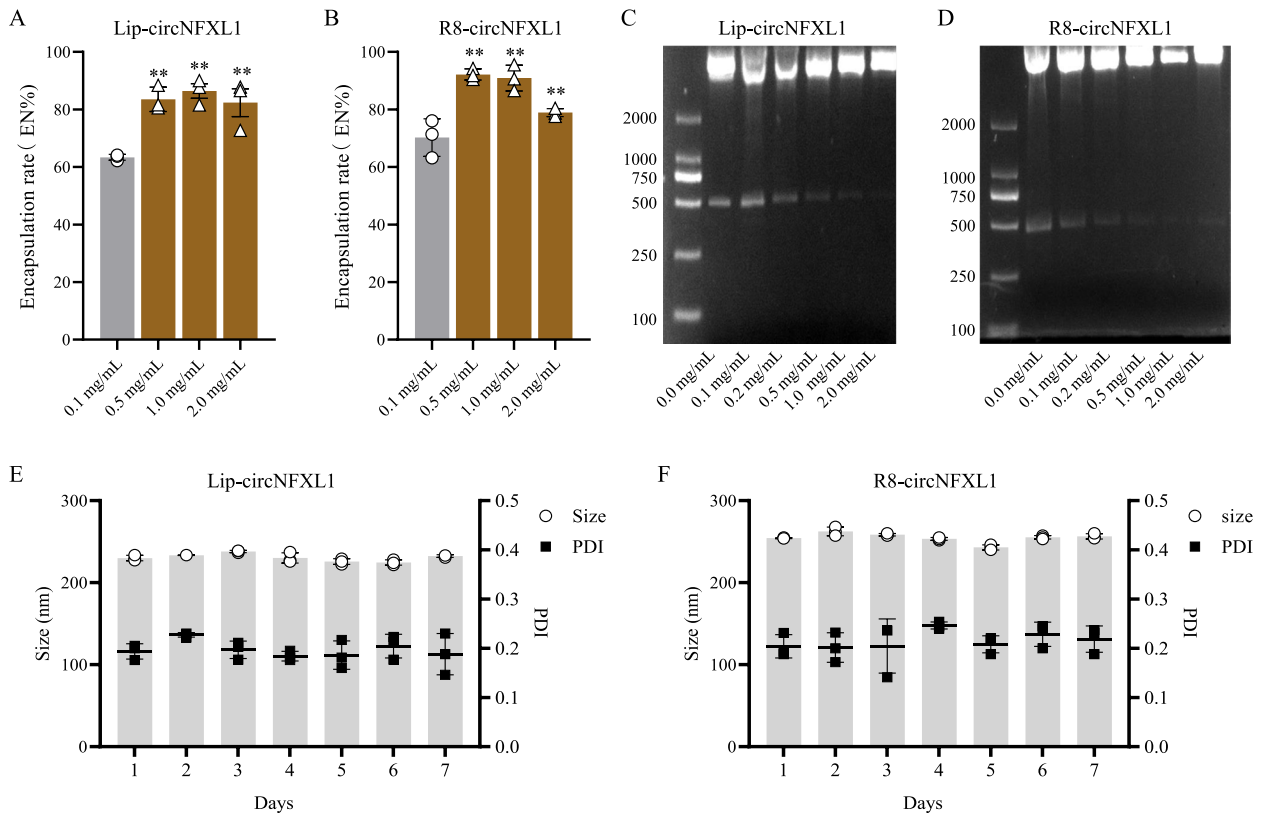

Fig. 2 Encapsulation Efficiency and Enzymatic Stability of Liposomal circNFXL1 Formulations. Encapsulation efficiency percentages of Lip-circNFXL1 (**A**) and R8-circNFXL1 (**B**) at various concentrations (0.1, 0.5, 1.0, and 2.0 mg/mL). Agarose gel electrophoresis results show the integrity of circNFXL1 (**C**) within Lip-circNFXL1 and R8-circNFXL1 (**D**) formulations after exposure to EcoRI and BamHI enzymes. Zeta potential measurements (mV) of Lip-circNFXL1 (**E**) and R8-circNFXL1 (**F**) formulations, illustrating electrostatic stability. Data are presented as mean ± SEM. Statistical comparisons were conducted using one-way ANOVA, followed by Bonferroni's post hoc test for multiple group comparisons. $^{**}p < 0.01$ compared to the 0.1 mg/mL group. **A**, **B**: n = 3 independent experiments; **E**, **F**: n = 7 per group

Resistance to enzymatic digestion was significantly enhanced with increasing concentrations of encapsulated circNFXL1. Notably, at 2 mg/mL, no degradation of circNFXL1 was observed (Fig. 2C, D), indicating that liposomal encapsulation effectively shields circNFXL1 from enzymatic breakdown, thereby improving its stability and potential bioavailability in vivo. Stability studies conducted over 7 days at 4 °C revealed that both Lip-circNFXL1 and R8-circNFXL1 maintained consistent particle sizes and low polydispersity indices (PDIs) (Fig. 2E, F). Hemolysis assays were performed to assess the biocompatibility of Lip-circNFXL1 and R8-circNFXL1 with red blood cells (RBC). As shown in Fig. 3A, both formulations exhibited minimal hemolytic activity. At concentrations up to 1 mg/mL, hemolysis rates for Lip-circNFXL1 and R8-circNFXL1 remained below 5% (Fig. 3B, C). To further evaluate safety, histological analyses were conducted on major organs, including the heart, liver, spleen, lungs, and kidneys, from both untreated control mice and those treated with liposomal circNFXL1 formulations. As shown in Fig. 3D, there were no significant histopathological differences between control and treated groups in any of the examined tissues.

Lung-targeting efficiency and organ distribution of intranasal delivery of R8-circNFXL1 in mice

To evaluate the lung-targeting efficiency and biodistribution of intranasally delivered R8-circNFXL1, a 0.5 mg/mL dose was selected based on its high

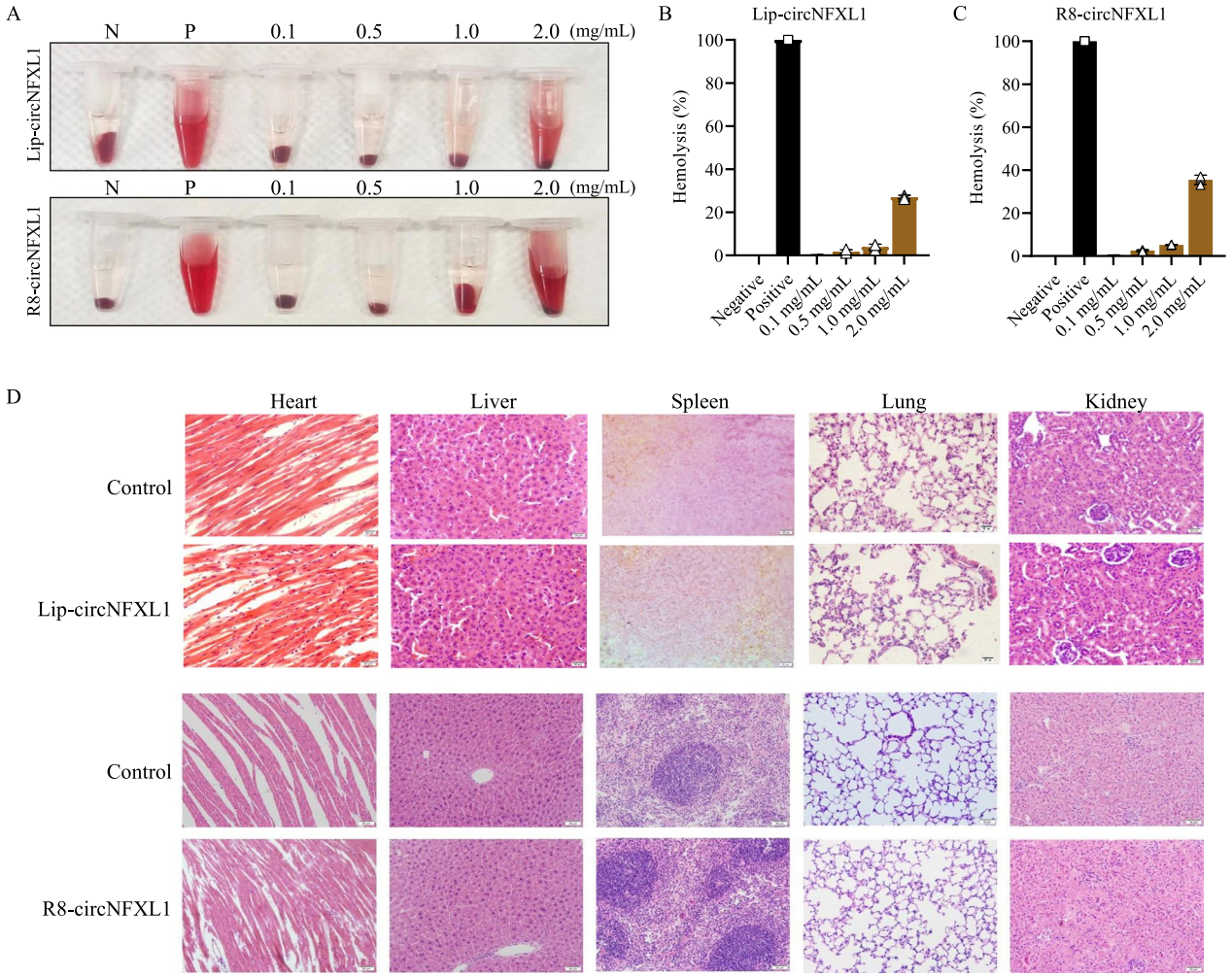

Fig. 3 Biocompatibility and Safety Profile of Liposomal circNFXL1 Formulations. **A** Hemolysis assays demonstrating the compatibility of Lip-circNFXL1 and R8-circNFXL1 with red blood cells. Quantitative analysis of hemolysis percentages for Lip-circNFXL1 (n = 3 independent experiments) (**B**) and R8-circNFXL1 (n = 3 independent experiments) (**C**) formulations at different concentrations. Negative control: PBS; Positive control: H_2O. **D** Histopathological evaluation of major organs (heart, liver, spleen, lung, and kidney) from mice treated with Lip-circNFXL1 and R8-circNFXL1 compared to untreated controls

encapsulation efficiency and low hemolysis rate, ensuring effective pulmonary delivery while maintaining biocompatibility. R8-circNFXL1, labeled with the near-infrared (NIR) fluorophore DID, was administered to mice either intravenously (Fig. 4A) or intranasally (Fig. 4B). Biodistribution and targeting efficiency were evaluated through in vivo fluorescence imaging over 24 h. Following intranasal delivery, strong fluorescence signals

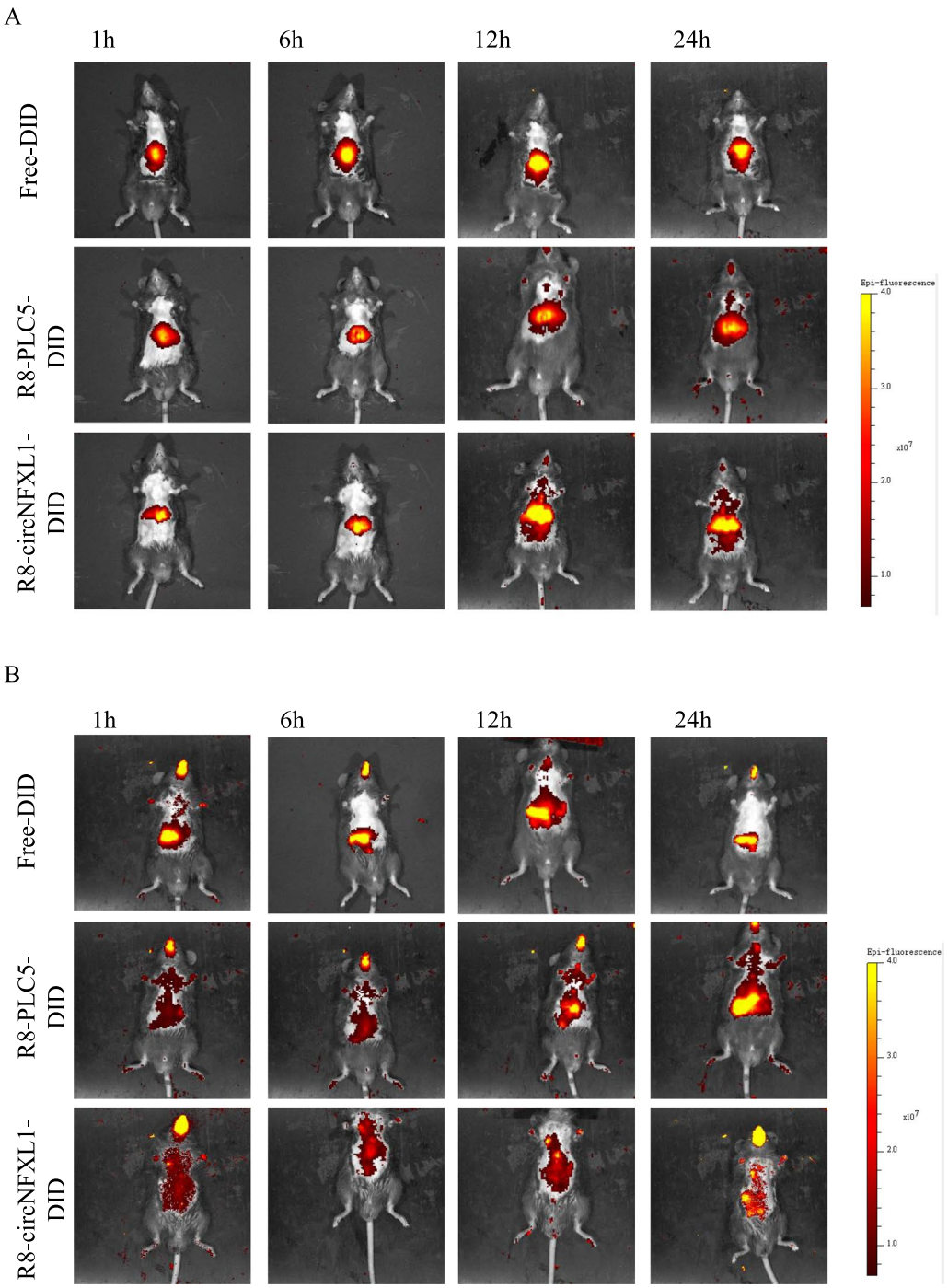

Fig. 4 In vivo Biodistribution of Liposomal circNFXL1 via Intravenous and Intranasal Administration in Mice. Representative fluorescence images showing the biodistribution of R8-circNFXL1, R8-PLC5-DID, and free DID dye in C57BL/6 mice at various time points (1, 6, 12, and 24 h) following **A** intravenous and **B** intranasal administration

appeared in the thoracic region within 1 h, indicating rapid localization to the lungs. The fluorescence intensity peaked shortly afterward and remained stable throughout the 24-h monitoring period, suggesting sustained retention within lung tissue (Fig. 4A, B).

To further analyze organ-specific accumulation, major organs, including the lungs, liver, spleen, kidneys, and heart, were harvested after 24 h and examined via ex vivo imaging (Fig. 5). Fluorescence intensity data revealed significantly stronger signals in the intranasal R8-circNFXL1 group (Fig. 5B) compared to the intravenous group (Fig. 5A). The intranasal R8-circNFXL1 delivery showed the highest fluorescence intensity in lung tissue, confirming effective targeting and tissue penetration enhanced by the R8 peptide. Minimal fluorescence was detected in off-target organs such as the brain, heart, and kidneys, demonstrating the specificity of the R8-circNFXL1 formulation for pulmonary tissue.

Therapeutic efficacy of intranasal delivery of R8-circNFXL1 in a mouse model of pulmonary arterial hypertension

We evaluated the therapeutic potential of intranasally delivered R8-circNFXL1 in a PAH mouse model induced by hypoxia and Su5416. Disease severity and treatment

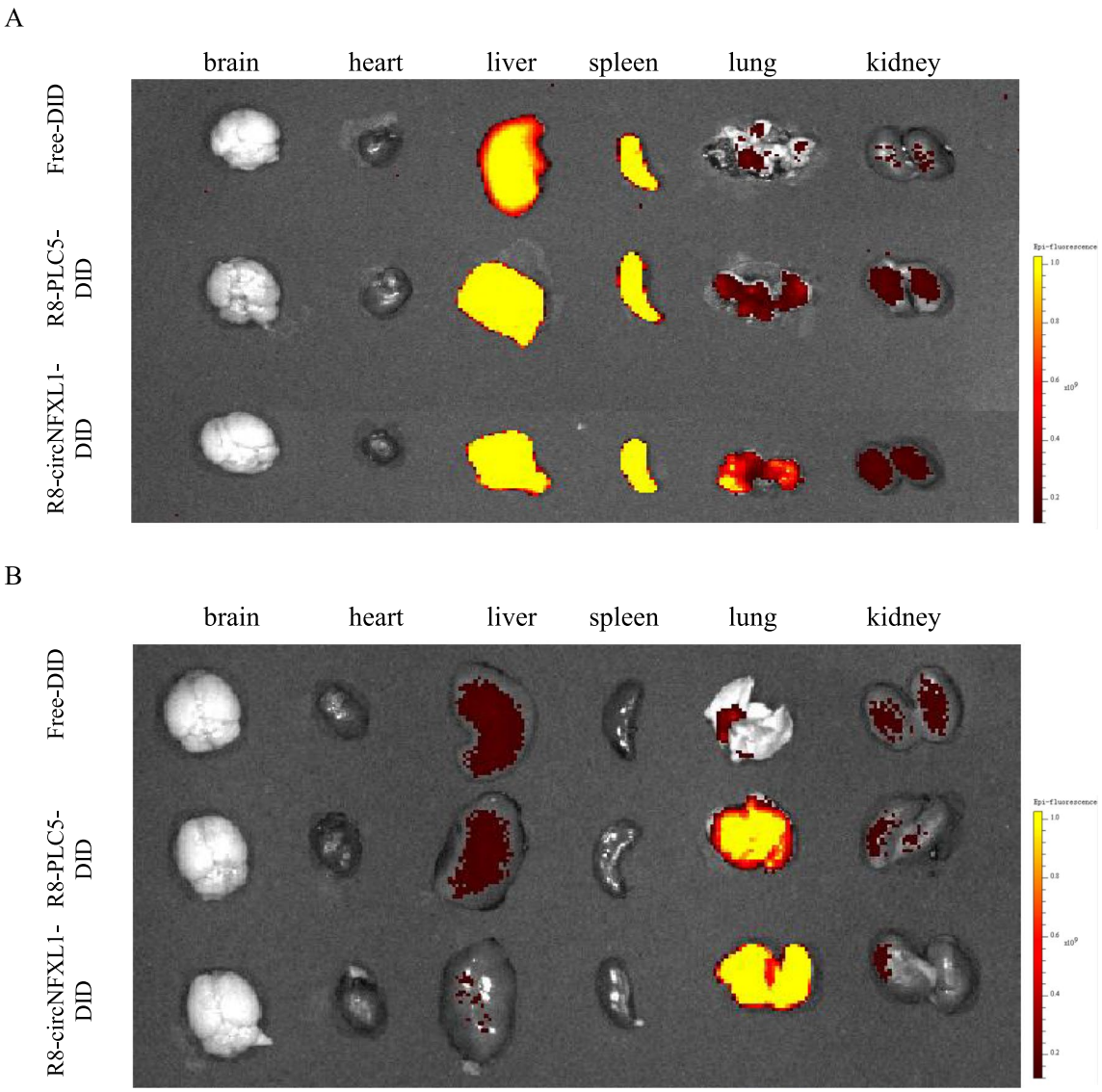

Fig. 5 Ex vivo Biodistribution of Liposomal circNFXL1 in Mice Following Intravenous and Intranasal Administration. Representative fluorescence images showing the ex vivo biodistribution of R8-circNFXL1, R8-PLC5-DID, and free DID dye in major organs (brain, heart, liver, spleen, lungs, and kidneys) of C57BL/6 mice at 24 h post-administration following **A** intravenous and **B** intranasal administration

efficacy were assessed using echocardiography and RV analysis (Fig. 6A). Successful PAH induction was confirmed by a significant increase in the Fulton index, expressed as the ratio of RV weight to the combined weight of the left ventricle and septum (RV/LV + S). PAH mice exhibited pronounced RVH, as indicated by an elevated RV/LV + S ratio (PAH = 0.61 ± 0.03 vs. Normal = 0.32 ± 0.01; $p < 0.0001$) (Fig. 6C). Treatment with R8-circNFXL1 significantly reduced RVH, lowering the RV/LV + S ratio in treated mice (R8-circNFXL1 = 0.42 ± 0.02 vs. PAH = 0.61 ± 0.03; $p < 0.0001$), suggesting effective mitigation of PAH-induced hypertrophic responses.

On day 21 post-PAH induction, echocardiographic measurements revealed substantial impairment in pulmonary artery function and RV performance in the PAH group (Fig. 6B). PAH mice showed reduced PAT (PAH = 14.58 ± 0.72 ms vs. Normal = 26.46 ± 1.94 ms; $p < 0.0001$) and PET (PAH = 64.37 ± 2.51 ms vs. Normal = 71.88 ± 4.80 ms; $p < 0.01$), indicating increased pulmonary vascular resistance. R8-circNFXL1 treatment significantly improved both PAT (20.21 ± 0.62 ms; $p < 0.001$ vs. PAH) and PET (69.38 ± 2.27 ms; $p < 0.05$ vs. PAH) (Fig. 6D), suggesting a reduction in vascular resistance. Additionally, the PAT/PET ratio, a key marker of pulmonary hypertension severity, was markedly reduced in the PAH group (0.23 ± 0.01) compared to the Normal group (0.37 ± 0.02; $p < 0.0001$). R8-circNFXL1 treatment significantly increased this ratio to 0.29 ± 0.01 ($p < 0.001$ vs. PAH) (Fig. 6E).

In PAH mice, PAVTI and PVmax were significantly diminished, with PAVTI dropping from 35.91 ± 2.03 cm in the Normal group to 19.32 ± 2.17 cm ($p < 0.0001$), and PVmax declining from 745.12 ± 43.78 mm/s to 541.95 ± 15.22 mm/s ($p < 0.0001$). R8-circNFXL1 treatment significantly improved both PAVTI (28.80 ± 2.75 cm; $p < 0.001$ vs. PAH) (Fig. 6F) and PVmax (664.68 ± 42.88 mm/s; $p < 0.001$ vs. PAH) (Fig. 6G), reflecting enhanced pulmonary blood flow and vascular function. Furthermore, PAH markedly impaired RV function, as indicated by reductions in TAPSE and CO, with TAPSE and CO values in the PAH group reaching 0.52 ± 0.08 mm and 3.71 ± 0.82 L/min, respectively, compared to 1.10 ± 0.10 mm and 13.07 ± 0.82 L/min in the Normal group ($p < 0.0001$ for both). R8-circNFXL1 treatment significantly restored TAPSE (0.96 ± 0.12 mm; $p < 0.001$ vs. PAH) (Fig. 6H) and CO (8.79 ± 0.72 L/min; $p < 0.001$ vs. PAH) (Fig. 6I). These findings suggested that R8-circNFXL1 provides substantial therapeutic benefits in the PAH model, effectively reducing RV hypertrophy, decreasing pulmonary vascular resistance, enhancing blood flow, and restoring RV function.

Effects of intranasal delivery of R8-circNFXL1 on pulmonary vascular remodeling and right ventricular hypertrophy in a PAH mouse model

After a 2-week treatment with intranasally delivered R8-circNFXL1, histological and immunohistochemical analyses were performed on lung and heart tissues to assess its therapeutic impact on PAH progression and RVH (Fig. 7). Pulmonary vascular remodeling and α-SMA expression were evaluated through H&E staining and α-SMA immunofluorescence, revealing distinct morphological differences among groups. The normal group exhibited open, unobstructed pulmonary vessels, indicative of healthy vascular structure. In contrast, the PAH group displayed markedly narrowed and thickened vessel walls with intense α-SMA expression, underscoring severe vascular remodeling and smooth muscle proliferation characteristic of PAH (Fig. 7A, D).

In the R8-circNFXL1 treatment group, vascular morphology showed partial restoration, with reduced wall thickness and moderately decreased α-SMA expression relative to the PAH group (Fig. 7C, E), suggesting that R8-circNFXL1 treatment effectively attenuates PAH-associated vascular remodeling. Right ventricular hypertrophy was quantified by assessing the right ventricular mass index, further supported by H&E staining of heart sections. The PAH group demonstrated a significant increase in RV mass (Fig. 7A, B), consistent with PAH-induced RV hypertrophy. However, R8-circNFXL1-treated mice showed a marked

(See figure on next page.)

Fig. 6 Therapeutic Efficacy of R8-circNFXL1 in a Mouse Model of Pulmonary Arterial Hypertension (PAH). **A** Experimental timeline illustrating PAH induction in mice using hypoxia and Su5416, followed by treatment with R8-circNFXL1. **B** Representative echocardiographic images and quantitative analyses of pulmonary and right ventricular (RV) function across different groups. **B** Doppler echocardiography depicting pulmonary artery acceleration time (PAT) and ejection time (PET), with the control, PAH, and R8-circNFXL1 treatment groups shown (*upper*). Representative M-mode echocardiographic images showing the right ventricular structure in each group (*lower*). **C** Quantitative measurement of RV/LV+S ratio (Fulton index), a marker of RV hypertrophy, in control, PAH, and R8-circNFXL1 treatment groups. Quantification of PAT (**D**), PAT/PET ratio (**E**), PAVTI (pulmonary artery velocity–time integral) (**F**), PVmax (peak velocity) (**G**), TAPSE (tricuspid annular plane systolic excursion) (**H**) and CO (cardiac output) (**I**) in control, PAH, and R8-circNFXL1 treatment groups. Data are presented as mean ± SEM. Statistical comparisons were performed using one-way ANOVA, followed by Bonferroni's post hoc test for multiple group comparisons. $^{**}p < 0.01$, $^{***}p < 0.001$ compared to Nor group, $^{\#}p < 0.05$, $^{\#\#}p < 0.01$ compared to PAH group (n = 3–6 per group)

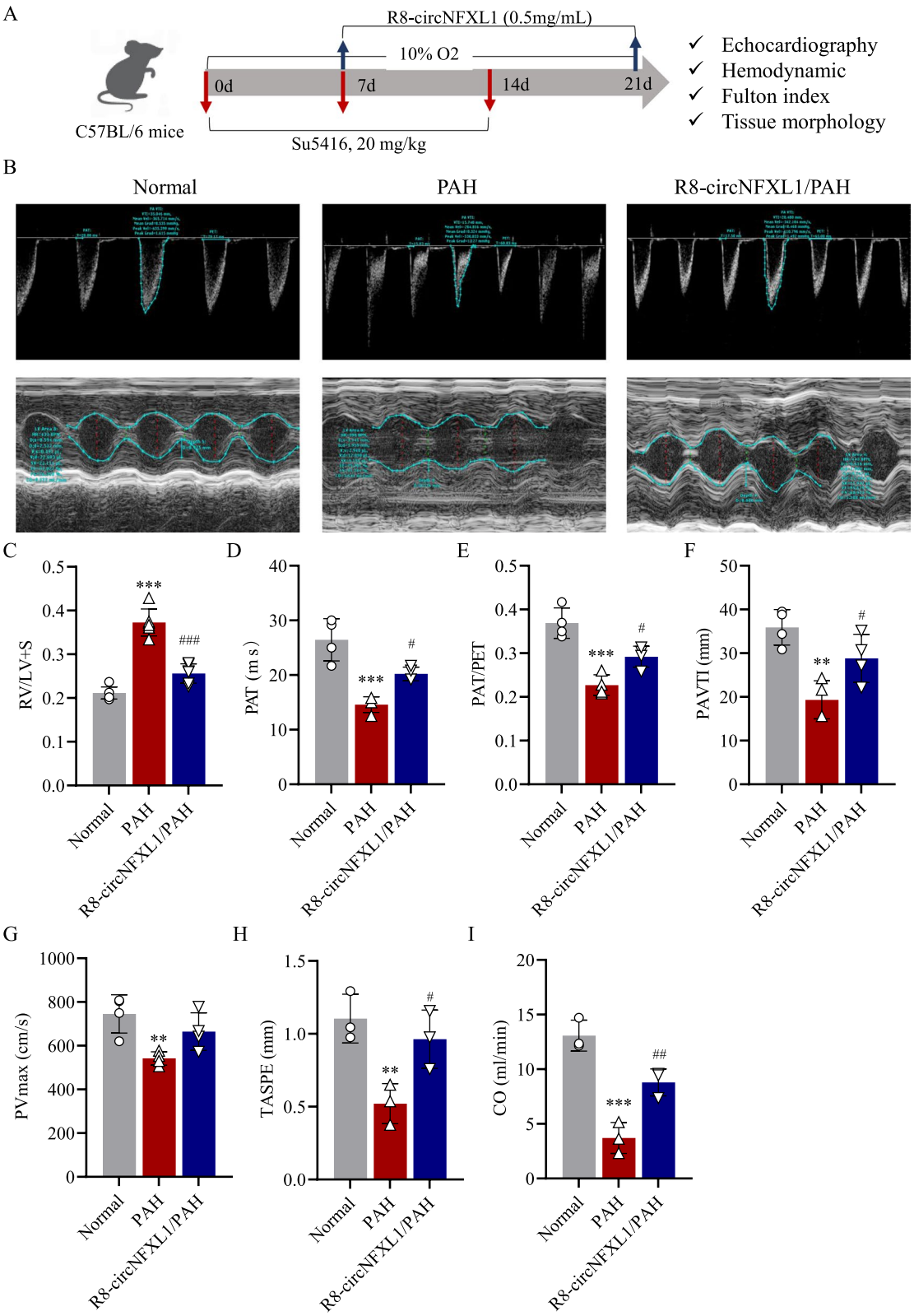

Fig. 6 (See legend on previous page.)

reduction in RV mass compared to the untreated PAH group (Fig. 7B), indicating that R8-circNFXL1 mitigates the hypertrophic response in the right ventricle. These findings demonstrated that R8-circNFXL1 treatment exerts beneficial effects on both pulmonary vascular remodeling and RV hypertrophy in the PAH mouse model, underscoring its potential therapeutic role in addressing PAH pathophysiology.

Modulation of the miR-29b/Kcnb1 axis by intranasal delivery of R8-circNFXL1 in a PAH mouse model

In our previous work, CircNFXL1 was identified as a molecular sponge for miR-29b, a microRNA associated with vascular remodeling, with Kcnb1 as a downstream target. Here, we examined expression levels of circNFXL1, miR-29b, and Kcnb1 across experimental groups using qRT-PCR and Western blot analyses. qRT-PCR results indicated a significant decrease in circNFXL1 expression in the PAH group (Fig. 7F), along with a marked upregulation of miR-29b relative to the normal control (Fig. 7G). Treatment with R8-circNFXL1 significantly reduced miR-29b levels in the PAH model, supporting circNFXL1's role in modulating miR-29b via miRNA sponging (Fig. 7G). Kcnb1 expression, notably downregulated in the PAH group (consistent with miR-29b's inhibitory influence), was partially restored with R8-circNFXL1 treatment (Fig. 7H, I). Further validation of R8-circNFXL1's modulatory effect on the miR-29b/Kcnb1 axis was provided by fluorescence intensity analysis. Immunofluorescence staining revealed the lowest levels of circNFXL1 and Kcnb1 in the PAH group, coupled with elevated miR-29b fluorescence, indicating its upregulation in response to PAH-induced vascular remodeling (Fig. 8A–D). In contrast, the R8-circNFXL1-treated group exhibited substantial increases in circNFXL1 and Kcnb1 fluorescence intensity, suggesting effective restoration of expression.

Discussion

PAH is a progressive disease characterized by pathological remodeling of pulmonary arteries, which increases vascular resistance, promotes right ventricular hypertrophy, and ultimately leads to heart failure [19]. A key driver of this remodeling is the excessive proliferation of vascular smooth muscle cells, which thicken and stiffen the vessel walls, restricting blood flow [20]. In our study, we introduce a novel therapeutic strategy using intranasal delivery of liposomal circNFXL1, a circular RNA capable of modulating the pathological remodeling processes in PAH. CircNFXL1 acts as a molecular sponge for miR-29b, a microRNA known to promote VSMC proliferation and migration. Additionally, circNFXL1 targets KCNB1, a gene encoding an ion channel crucial for vascular homeostasis [13]. By modulating the miR-29b/KCNB1 axis, circNFXL1 provides a targeted approach to counteract the vascular remodeling central to PAH pathology. This approach has the potential to specifically address the underlying cellular mechanisms driving PAH progression, highlighting circNFXL1 as a promising candidate for future therapeutic development.

In this study, we successfully developed an R8-modified liposomal delivery system encapsulating circNFXL1 via a thin-film hydration method, achieving a formulation with optimal physicochemical properties for targeted pulmonary delivery. The R8 peptide, a well-established cell-penetrating peptide, was selected for its demonstrated ability to enhance cellular uptake and tissue penetration [17], particularly within the lungs [21]. Previous studies have shown that R8 modifications improve nanoparticle targeting and retention in lung tissue due to the peptide's positive charge and its interaction with negatively charged cellular membranes, facilitating translocation across biological barriers and enhancing accumulation in lung capillaries [21]. In our study, transmission electron microscopy and dynamic light scattering analyses confirmed the formation of uniform, spherical particles, with a size range of 200–300 nm—ideal for pulmonary delivery. Nanoparticles within this range can efficiently bypass alveolar macrophages, prolonging retention in lung tissue and enhancing therapeutic efficacy [22]. Our R8-circNFXL1 formulation demonstrated high encapsulation efficiency and notable resistance to enzymatic degradation, suggesting its stability and potential bioavailability in the pulmonary system. These characteristics, particularly the R8-modified formulation's stability and lung-targeting

(See figure on next page.)

Fig. 7 Effects of R8-circNFXL1 on Pulmonary Vascular Remodeling and Right Ventricular Hypertrophy in a PAH Mouse Model. **A** Representative HE staining of lung sections illustrating the heart morphology across experimental groups (*upper*). Higher magnification HE images of lung sections highlighting detailed structural differences in vascular morphology and remodeling severity across groups (*lower*). Quantification of length of RV (**B**) and vessel wall thickness of pulmonary artery (**C**) across groups. **D** Immunofluorescence staining for α-SMA (*red*), circNFXL1 (*green*), and nuclei (*blue*) in lung sections across groups. **E** Quantification of the expression of circNFXL1 across groups. qRT-PCR analysis of circNFXL1 (**F**), miR-29b (**G**), and Kcnb1 (**H**) expression levels in pulmonary artery tissues. **I** Western blot analysis and quantification of KCNB1 protein levels. Data are presented as mean ± SEM. Statistical comparisons were conducted using one-way ANOVA, followed by Bonferroni's post hoc test for multiple group comparisons. $^{**}p < 0.01$, $^{***}p < 0.001$ compared to Nor group, $^{\#}p < 0.05$, $^{\#\#}p < 0.01$, $^{\#\#\#}p < 0.001$ compared to PAH group (n = 4–9 per group)

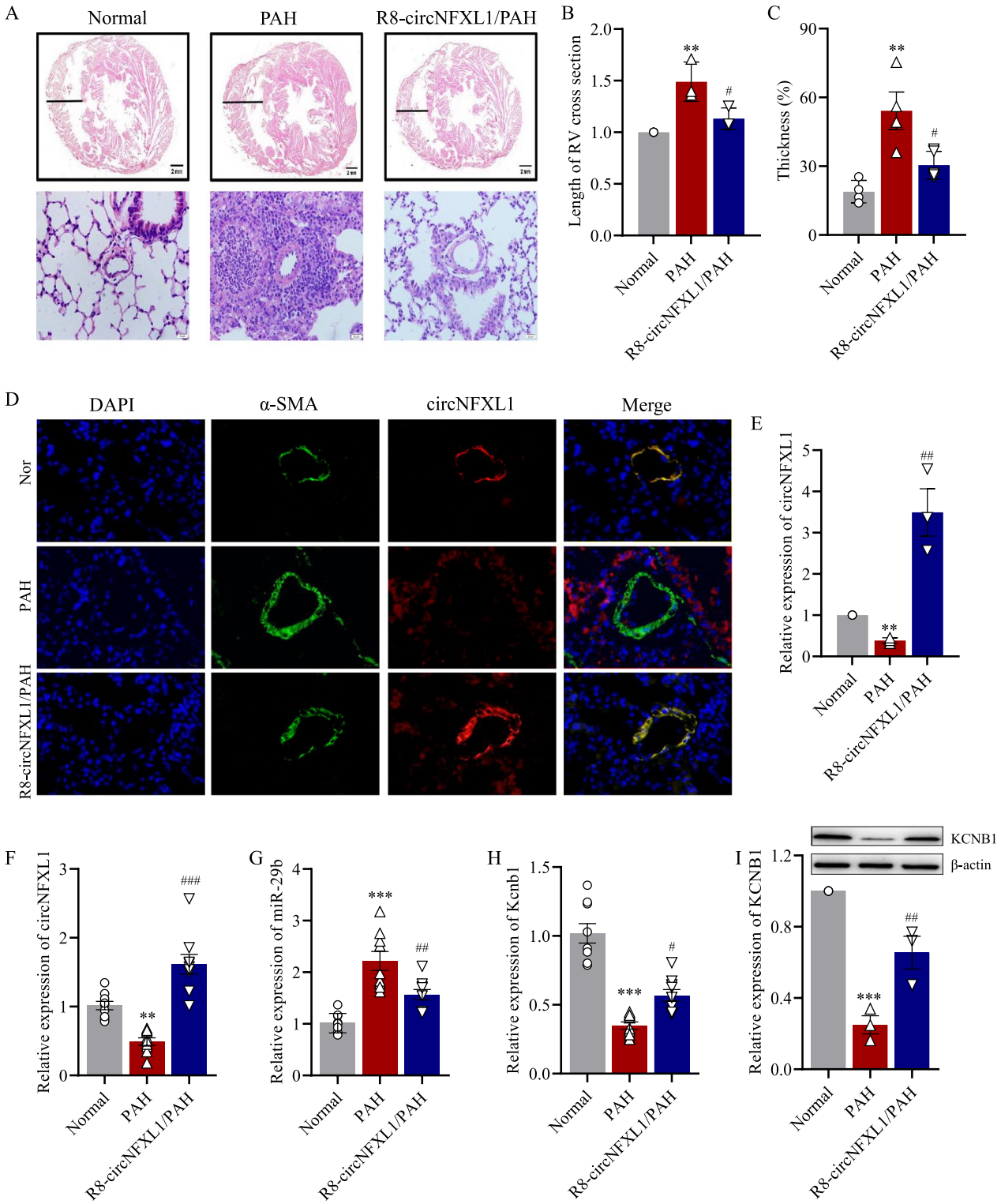

Fig. 7 (See legend on previous page.)

efficiency, offer significant advantages over conventional liposomal delivery systems. The high encapsulation efficiency ensures that a substantial therapeutic dose of circNFXL1 reaches pulmonary tissues. These results revealed strong localization of the liposomes in the lungs with minimal off-target accumulation, highlighting

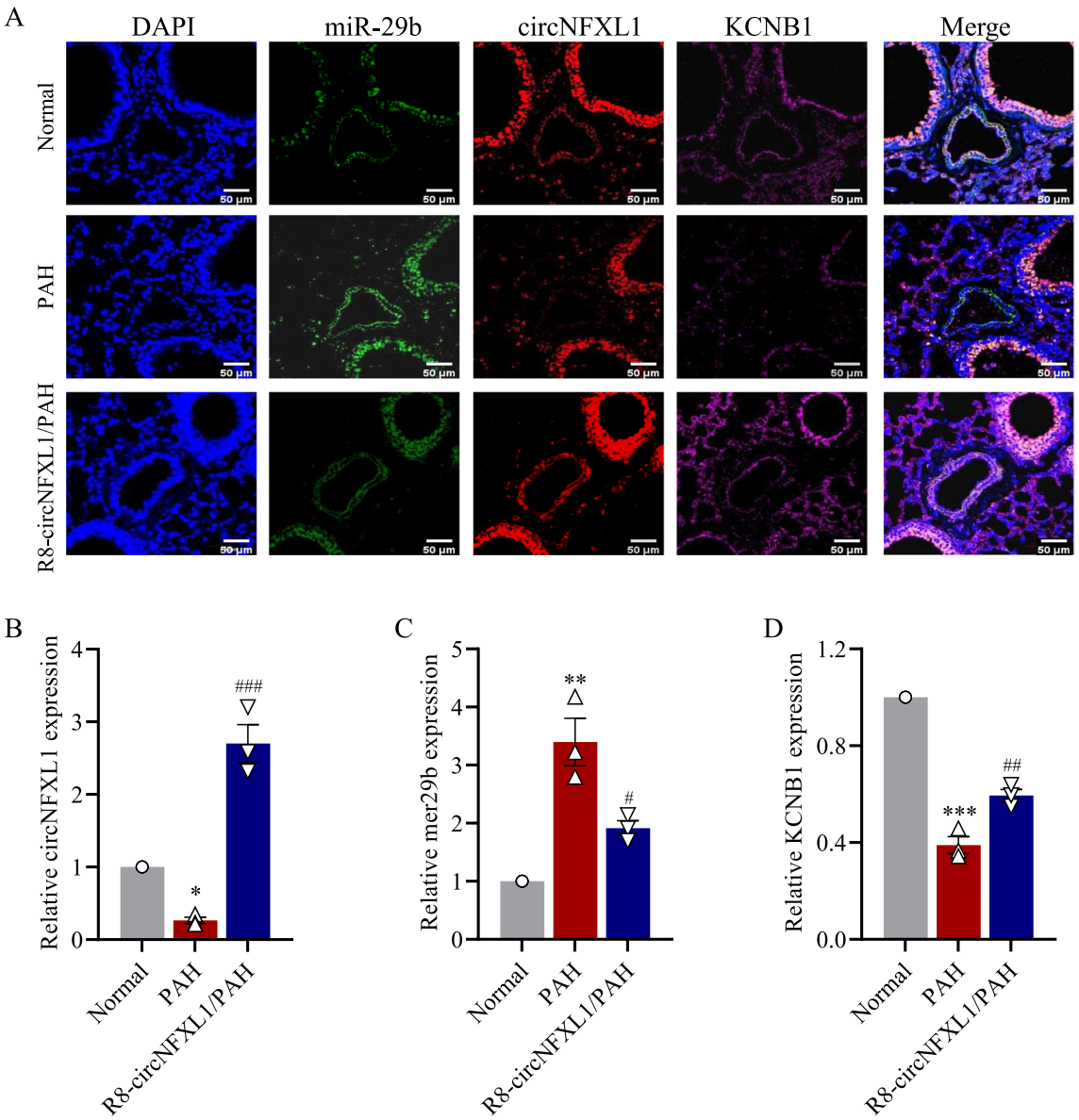

Fig. 8 Modulation of the miR-29b/Kcnb1 Axis by R8-circNFXL1 in Pulmonary Arterial Hypertension (PAH). **A** Immunofluorescence staining of lung tissues showing circNFXL1 (*green*), miR-29b (*red*), Kcnb1 (*purple*), and DAPI (*blue*) across different experimental groups: Normal (Nor), PAH, and PAH with R8-circNFXL1 treatment. Quantitative analysis of fluorescence intensity for circNFXL1 (**B**), miR-29b (**C**), and KCNB1 (**D**) in pulmonary artery tissue sections across groups. Data are presented as mean ± SEM. Statistical comparisons were conducted using one-way ANOVA, followed by Bonferroni's post hoc test for multiple group comparisons. *$p < 0.05$, **$p < 0.01$, ***$p < 0.001$ compared to Nor group, $^{\#}p < 0.05$, $^{\#\#}p < 0.01$, $^{\#\#\#}p < 0.001$ compared to PAH group (n = 3 per group)

the potential for focused pulmonary delivery with reduced systemic exposure and adverse effects in non-target organs. We also chose intranasal administration for R8-circNFXL1 to maximize respiratory tract bioavailability, bypassing gastrointestinal and hepatic first-pass metabolism. This route allows for higher localized drug concentrations in the pulmonary system [23–25]. Biodistribution studies validated the lung-targeting capabilities of R8-circNFXL1, with near-infrared fluorescence imaging showing rapid lung accumulation within one hour of administration and sustained retention for up to 24 h. Ex vivo imaging confirmed predominant lung localization with minimal off-target distribution, particularly in comparison to the liver and spleen, where only moderate accumulation was observed. Together, the R8-circNFXL1 formulation's

targeting efficiency, high encapsulation rate, stability, and sustained lung retention position it as a promising candidate for localized PAH therapy. These findings support further investigation into R8-circNFXL1 for clinical applications in PAH, leveraging R8-mediated delivery for effective and focused therapeutic outcomes.

In this study, the 0.5 mg/mL dosage of R8-circNFXL1 was selected to achieve an optimal balance between encapsulation efficiency and hemolysis safety. Our liposome characterization studies demonstrated that at this concentration, encapsulation efficiency remained high, ensuring that a sufficient amount of circNFXL1 was delivered to the target pulmonary tissues. Additionally, hemolysis assays confirmed that the 0.5 mg/mL dose exhibited minimal hemolytic activity, supporting its biocompatibility and safety for intranasal administration. Given these findings, the 0.5 mg/mL dose was chosen as the optimal concentration to study the lung-targeting efficiency and biodistribution of intranasally delivered R8-circNFXL1, allowing for maximal pulmonary localization while minimizing systemic toxicity. Future studies will further refine dose optimization and pharmacokinetic modeling to ensure long-term therapeutic effectiveness while addressing potential interindividual variability in nasal absorption and clearance.

Furthermore, the therapeutic efficacy of R8-circNFXL1 was evaluated in a Su5416 and hypoxia-induced PAH mouse model, which accurately replicates human PAH pathology, including vascular remodeling and right ventricular hypertrophy [26]. Our results demonstrated a significant therapeutic effect, as evidenced by decreased right ventricular hypertrophy, improved pulmonary vascular resistance, and restored right ventricular function. Histological analyses indicated a reduction in pulmonary artery wall thickness and α-SMA expression in R8-circNFXL1-treated mice compared to untreated PAH mice, suggesting that the treatment attenuates the VSMC proliferation and vessel thickening typical of PAH. This outcome highlights R8-circNFXL1's potential to directly counteract the vascular remodeling processes that drive PAH progression. At the molecular level, R8-circNFXL1 treatment modulated the miR-29b/KCNB1 axis, further confirming its therapeutic potential. PAH is associated with elevated miR-29b levels [13, 27, 28], which promote VSMC proliferation and inhibit KCNB1 expression, disrupting ion homeostasis in pulmonary arteries. The R8-circNFXL1 treatment effectively reduced miR-29b expression and partially restored KCNB1 levels, reversing the molecular alterations induced by PAH. Immunofluorescence staining also confirmed these findings, with increased fluorescence intensity of circNFXL1 and KCNB1 in R8-circNFXL1-treated lungs, suggesting that circNFXL1's miRNA sponging activity successfully mitigates miR-29b's pathological impact on VSMC. This finding aligns with circNFXL1's observed modulatory effects on the miR-29b/KCNB1 axis, supporting the notion that its therapeutic action in PAH is likely mediated by miRNA regulation. However, several limitations warrant consideration. The Su5416-hypoxia PAH model, although widely accepted, does not fully replicate the complexity of human PAH, which may limit the translatability of our findings. Additionally, our study's short duration may not capture the long-term effects and potential side effects of R8-circNFXL1 therapy. Future studies should consider exploring dose optimization, immune response assessments, and longer treatment durations. Furthermore, while intranasal delivery enhances pulmonary targeting, variability in nasal absorption rates could influence therapeutic outcomes, necessitating further pharmacokinetic and pharmacodynamic evaluations in clinical contexts.

Current PAH therapies, including prostacyclin analogs, PDE-5 inhibitors, and endothelin receptor antagonists, primarily function as vasodilators, reducing pulmonary arterial pressure to alleviate right ventricular overload. However, these treatments do not directly target the underlying vascular remodeling processes that drive disease progression. Additionally, they are often limited by systemic side effects, short half-lives, and drug resistance, necessitating frequent dose adjustments and long-term management strategies. In contrast, R8-circNFXL1 offers a mechanistically distinct approach, directly modulating pathological signaling pathways involved in vascular remodeling and right ventricular hypertrophy. By specifically targeting VSMC proliferation and pulmonary artery remodeling through the miR-29b/KCNB1 axis, R8-circNFXL1 provides a potential disease-modifying effect, rather than simply managing hemodynamics. This mechanistic distinction suggests that R8-circNFXL1 could complement existing PAH treatments by addressing both functional and structural abnormalities in the pulmonary vasculature. Another key advantage of R8-circNFXL1 is its intranasal delivery system, which ensures localized pulmonary effects, reducing systemic exposure and off-target effects. Unlike current PAH therapies that require oral, intravenous, or subcutaneous administration, intranasal delivery is non-invasive and may offer more consistent pulmonary drug concentrations with reduced hepatic metabolism. Our biodistribution studies confirm strong pulmonary retention, suggesting that R8-circNFXL1 could provide sustained therapeutic effects with fewer systemic side effects. Given these advantages, future studies should explore the combination of R8-circNFXL1 with existing PAH therapies to assess potential synergistic effects. By

integrating vasodilatory agents with molecularly targeted circRNA therapy, a multimodal treatment approach could be developed to achieve both symptomatic relief and long-term vascular remodeling reversal, ultimately improving clinical outcomes for PAH patients.

Despite the promising findings of this study, several limitations should be acknowledged. First, while the SuHx PAH model is widely used and effectively mimics key pathological features of human PAH, it does not fully capture the genetic, environmental, and hemodynamic complexities observed in patients. Second, the short duration of the study may not fully capture the long-term therapeutic effects and potential immune responses associated with R8-circNFXL1 treatment. Extended studies with chronic administration protocols are needed to evaluate long-term efficacy, safety, and immune compatibility, particularly in the context of repeated dosing and potential inflammatory or immunogenic responses. Third, the scalability and stability of R8-circNFXL1 remain key challenges for clinical translation. While our formulation demonstrated high encapsulation efficiency, pulmonary retention, and biological activity, large-scale production feasibility must be further optimized. Fourth, additional pharmacokinetic and pharmacodynamic studies are required to optimize intranasal delivery parameters, assess circNFXL1's bioavailability and degradation kinetics, and minimize interindividual variability in pulmonary absorption. While our biodistribution studies confirm effective pulmonary targeting, further in vitro release kinetics studies using relevant lung fluid models are warranted to evaluate the controlled release profile of circNFXL1 from R8-modified liposomes under physiological conditions. Finally, combination strategies with current PAH pharmacotherapies, such as prostacyclin analogs, PDE-5 inhibitors, and endothelin receptor antagonists, should be explored. Given the distinct molecular mechanism of R8-circNFXL1—targeting vascular remodeling rather than vasodilation alone—there is potential for synergistic effects when used in combination with existing treatments. Addressing these limitations will be essential for advancing R8-circNFXL1 toward clinical translation and further establishing its potential as a novel targeted therapy for PAH.

Conclusion

In conclusion, our study demonstrates that R8-circNFXL1 significantly ameliorates PAH-associated vascular remodeling and right ventricular hypertrophy through modulation of the miR-29b/KCNB1 axis. The successful targeting and retention of R8-circNFXL1 in lung tissue, combined with its non-invasive intranasal delivery route, make it a compelling candidate for clinical development. This approach exemplifies the therapeutic potential of circRNAs in addressing the molecular underpinnings of PAH, providing a foundation for further studies aimed at advancing non-coding RNA-based therapies for vascular diseases. Future investigations should build upon these findings, with a focus on optimizing delivery systems, extending clinical applicability, and exploring additional circRNA targets to expand the scope of circRNA-based interventions in PAH and beyond.

Supplementary Information

The online version contains supplementary material available at https://doi.org/10.1186/s12931-025-03203-y.

Additional file 1.

Author contributions

Acquisition of data: Miao Guo, Shan-Shan Li, Ying Zhao. Data analysis: Miao Guo, Shan-Shan Li, Ying Zhao, Feifei Fan, Shaoyuan Huang, Houzhi Yang, Xu Chen. Writing of the manuscript: Shan-Shan Li and Xin Jin. Review and/or revision of the manuscript: Shan-Shan Li and Xin Jin. Conception and design: Shan-Shan Li and Xin Jin. Study supervision: Shan-Shan Li and in Jin.

Funding

This research was funded by the National Natural Science Foundation of China, grant number 81971083; The Open Fund of Tianjin Central Hospital of Gynecology Obstetrics/Tianjin Key Laboratory of Human Development and Reproductive Regulation, grant number 2022XHY01.

Data availability

No datasets were generated or analysed during the current study.

Declarations

Ethics approval and consent to participate

All experimental protocols were carefully designed to minimize any potential distress or discomfort to the animals. These protocols were approved by the Nankai University Animal Care and Use Committee, following institutional guidelines for the ethical treatment of animals in research.

Consent for publication

Not applicable.

Competing interests

The authors declare no competing interests.

Author details

[1]School of Medicine, Nankai University, Tianjin, China. [2]Tianjin Central Hospital of Gynecology Obstetrics, Tianjin, China. [3]Tianjin Key Laboratory of Human Development and Reproductive Regulation, Tianjin, China. [4]Tianjin Medical University, Tianjin, China.

Received: 3 December 2024 Accepted: 26 March 2025
Published online: 06 April 2025

References

1. Ruopp NF, Cockrill BA. Diagnosis and treatment of pulmonary arterial hypertension: a review. JAMA. 2022;327(14):1379–91.
2. Hassoun PM. Pulmonary arterial hypertension. N Engl J Med. 2021;385(25):2361–76.

3. Naeije R, Richter MJ, Rubin LJ. The physiological basis of pulmonary arterial hypertension. Eur Respir J. 2022;59(6):2102334.
4. Johnson S, et al. Pulmonary hypertension: a contemporary review. Am J Respir Crit Care Med. 2023;208(5):528–48.
5. Guignabert C, Humbert M. Targeting transforming growth factor-beta receptors in pulmonary hypertension. Eur Respir J. 2021;57(2):2002341.
6. Klinger JR, et al. Therapy for pulmonary arterial hypertension in adults: update of the CHEST Guideline and Expert Panel Report. Chest. 2019;155(3):565–86.
7. Omura J, et al. Identification of long noncoding RNA H19 as a new biomarker and therapeutic target in right ventricular failure in pulmonary arterial hypertension. Circulation. 2020;142(15):1464–84.
8. Chen B, et al. Non-coding RNA networks in pulmonary arterial hypertension. Pharmacology. 2024. https://doi.org/10.1159/000541060.
9. Han Y, et al. Role of long non-coding RNAs in pulmonary arterial hypertension. Cells. 2021;10(8):1892.
10. Lu GF, et al. Reduced CircSMOC1 level promotes metabolic reprogramming via PTBP1 (polypyrimidine tract-binding protein) and miR-329-3p in pulmonary arterial hypertension rats. Hypertension. 2022;79(11):2465–79.
11. Farkas L, Goncharova EA. Circling in on pulmonary arterial hypertension: is it time to consider circular RNA circ_0016070 as a biomarker and target for therapy? J Am Heart Assoc. 2022;11(14): e026798.
12. Jiang Y, et al. Circular RNA Calm4 regulates hypoxia-induced pulmonary arterial smooth muscle cells pyroptosis via the Circ-Calm4/miR-124-3p/PDCD6 axis. Arterioscler Thromb Vasc Biol. 2021;41(5):1675–93.
13. Jin X, et al. hsa_circNFXL1_009 modulates apoptosis, proliferation, migration, and potassium channel activation in pulmonary hypertension. Mol Ther Nucleic Acids. 2021;23:1007–19.
14. Li SS, et al. circNFXL1 modulates the Kv2.1 channel function in hypoxic human pulmonary artery smooth muscle cells via sponging miR-29b-2–5p as a competitive endogenous RNA. J Cardiovasc Pharmacol. 2023;81(4):292–9.
15. Shah S, et al. Liposomes: advancements and innovation in the manufacturing process. Adv Drug Deliv Rev. 2020;154–155:102–22.
16. Guimaraes D, Cavaco-Paulo A, Nogueira E. Design of liposomes as drug delivery system for therapeutic applications. Int J Pharm. 2021;601: 120571.
17. Nakamura T, et al. Innovative nanotechnologies for enhancing nucleic acids/gene therapy: controlling intracellular trafficking to targeted biodistribution. Biomaterials. 2019;218: 119329.
18. Nakamura T, et al. Octaarginine-modified liposomes enhance cross-presentation by promoting the C-terminal trimming of antigen peptide. Mol Pharm. 2014;11(8):2787–95.
19. Prins KW, Thenappan T. World Health Organization Group I Pulmonary Hypertension: epidemiology and pathophysiology. Cardiol Clin. 2016;34(3):363–74.
20. Brown IAM, et al. Vascular smooth muscle remodeling in conductive and resistance arteries in hypertension. Arterioscler Thromb Vasc Biol. 2018;38(9):1969–85.
21. Hagino Y, et al. GALA-modified lipid nanoparticles for the targeted delivery of plasmid DNA to the lungs. Mol Pharm. 2021;18(3):878–88.
22. Menon JU, et al. Polymeric nanoparticles for pulmonary protein and DNA delivery. Acta Biomater. 2014;10(6):2643–52.
23. Pivniouk V, et al. Airway administration of OM-85, a bacterial lysate, blocks experimental asthma by targeting dendritic cells and the epithelium/IL-33/ILC2 axis. J Allergy Clin Immunol. 2022;149(3):943–56.
24. Nelson SA, Sant AJ. Potentiating lung mucosal immunity through intranasal vaccination. Front Immunol. 2021;12: 808527.
25. Feng KN, et al. IL-37 protects against airway remodeling by reversing bronchial epithelial-mesenchymal transition via IL-24 signaling pathway in chronic asthma. Respir Res. 2022;23(1):244.
26. Wu XH, et al. Experimental animal models of pulmonary hypertension: development and challenges. Animal Model Exp Med. 2022;5(3):207–16.
27. Cushing L, et al. Disruption of miR-29 leads to aberrant differentiation of smooth muscle cells selectively associated with distal lung vasculature. PLoS Genet. 2015;11(5): e1005238.
28. Wang T, et al. TGF-beta1/Smad3 signaling promotes collagen synthesis in pulmonary artery smooth muscle by down-regulating miR-29b. Int J Clin Exp Pathol. 2018;11(12):5592–601.

Publisher's Note